Supplementary Information

Intensity-asymmetric wavefront shaping in nonlocal meta-lens

Jin Yao,[1,†] Zhihui Wang,[1,†] Yubin Fan,[1,*] Ke Zhang,[1] Rong Lin,[1] Jiajun Wu,[1] Chang Peng,[1] Shumin Xiao,[2,3,*] and Din Ping Tsai[1,4,5,6,*]

[1] *Department of Electrical Engineering and State Key Laboratory of Optical Quantum Materials, City University of Hong Kong, Kowloon, Hong Kong SAR, China*

[2] *State Key Laboratory on Tunable Laser Technology, Ministry of Industry and Information Technology Key Lab of Micro-Nano Optoelectronic Information System, Shenzhen Graduate School, Harbin Institute of Technology, Shenzhen 518055, China*

[3] *Pengcheng Laboratory, Shenzhen, China*

[4] *Centre for Biosystems, Neuroscience, and Nanotechnology, City University of Hong Kong, Kowloon, Hong Kong SAR, China*

[5] *State Key Laboratory of Terahertz and Millimeter Waves, City University of Hong Kong, Kowloon, Hong Kong SAR, China*

[6] *Department of Physics, City University of Hong Kong, Kowloon, Hong Kong SAR, China*

[*]Corresponding Authors, E-mails: fanyb@pcl.ac.cn; shumin.xiao@hit.edu.cn; dptsai@cityu.edu.hk

[†]These authors contributed equally to this work.

Supplementary Note 1: Refractive index of silicon film

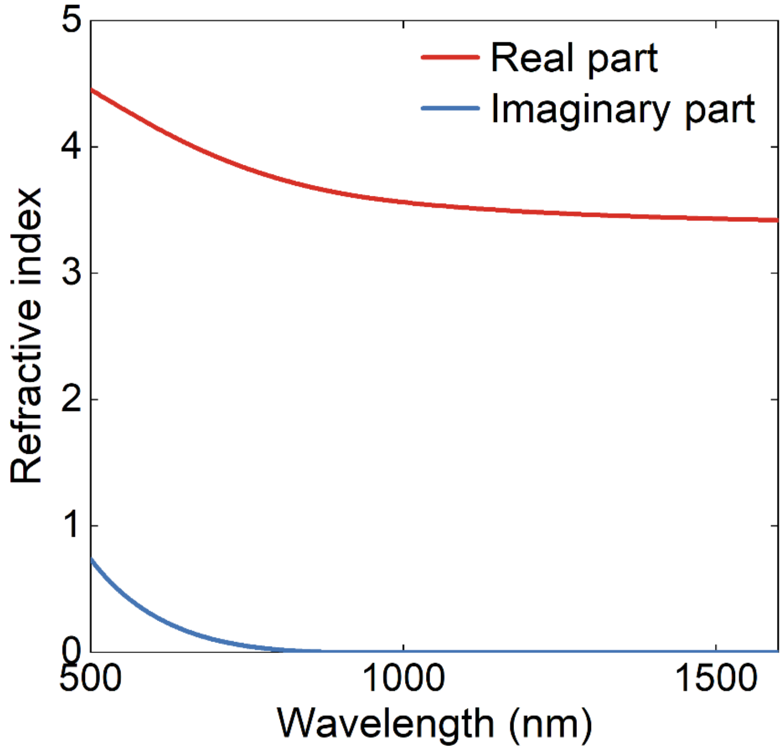

Supplementary Fig. 1: Complex refractive index of the silicon film. Wavelength-dependent real and imaginary refractive index components are extracted from spectroscopic ellipsometry.

Supplementary Note 2: Linear and nonlinear measurement setups

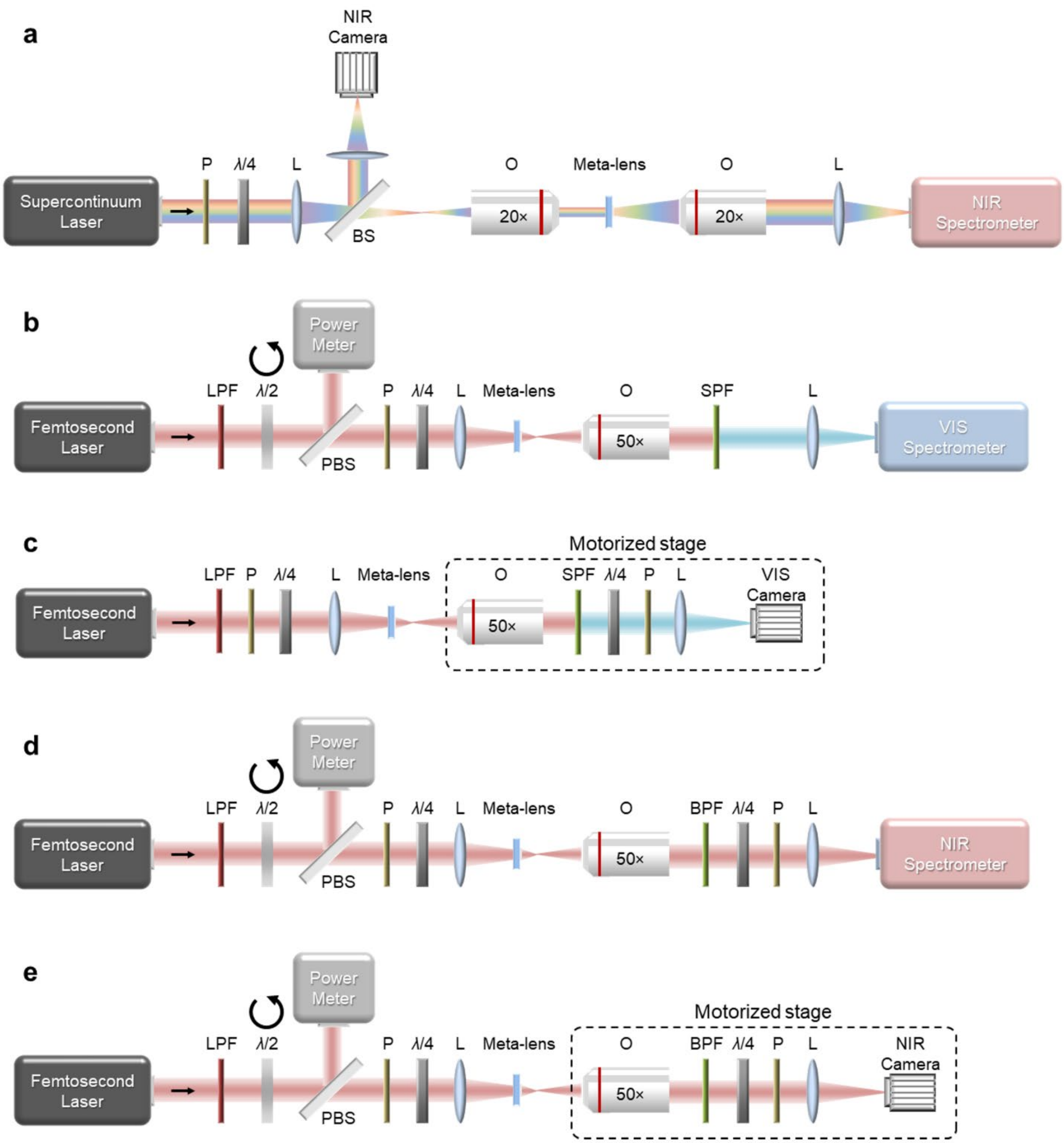

Supplementary Fig. 2: Schematics of linear and nonlinear measurement setups. a-e Optical measurement setups for linear transmission spectra (**a**), nonlinear spectra (**b**), harmonic-generation light-field profiles (**c**), intensity-dependent spectra (**d**), and intensity-dependent light-field profiles (**e**). P: Linear polarizer, L: Lens, BS: Beam splitter, PBS: Polarizing beam splitter, O: Objective, $\lambda/4$: Quarter-wave plate, $\lambda/2$: Half-wave plate, LPF: Long-pass filter, SPF: Short-pass filter, BPF: Band-pass filter.

Supplementary Note 3: Selection of quality factor

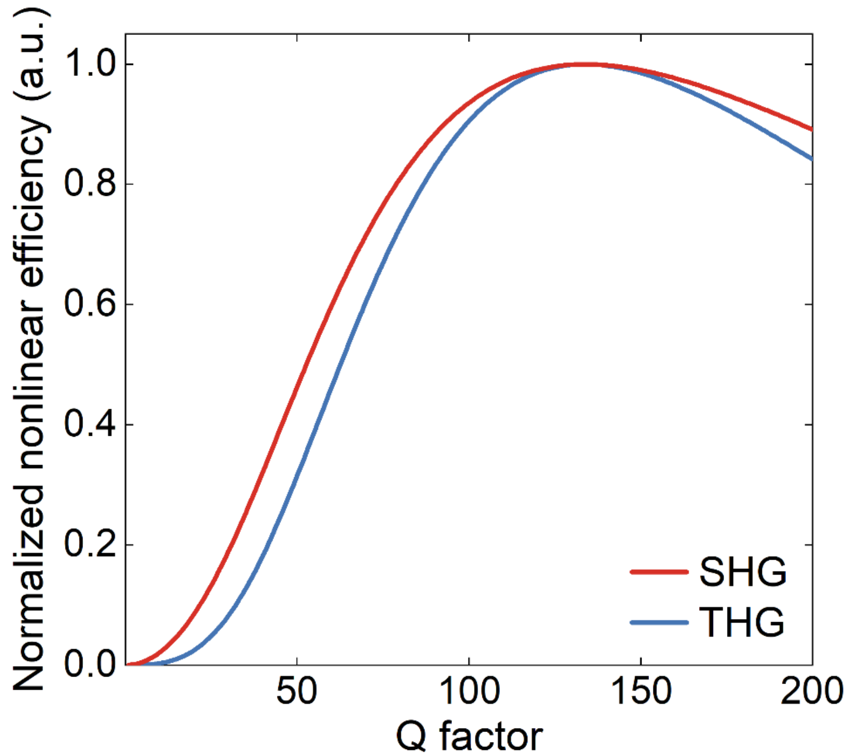

Supplementary Fig. 3: Selection of the quality factor. Normalized nonlinear second harmonic generation (SHG) and third harmonic generation (THG) efficiencies as a function of quality (Q) factor.

Since the pump source is a femtosecond pulsed laser, selecting an appropriate Q factor is crucial for optimizing nonlinear conversion. While a higher Q factor typically enhances the field buildup inside a resonator, an excessively high Q factor prevents the cavity from reaching its steady-state response within the limited pulse duration, thereby reducing the effective nonlinear interaction. This trade-off can be quantitatively analyzed by considering the cavity rise time τ, which determines how fast the resonance builds up. It is expressed as

$$\tau = \frac{Q\lambda}{2\pi c}, \tag{1}$$

where Q is the Q factor, λ = 1570 nm is the pump wavelength, and c is the speed of light. The electric field $E(t)$ gradually tends to the steady state in the cavity in an exponential relationship, described as

$$E(t) = E_{\mathrm{s}}\left[1 - e^{-(\frac{t}{\tau})}\right], \tag{2}$$

where E_{s} is the steady-state electric field amplitude, and t is time, corresponding to the pump pulse duration of 140 fs. For a given cavity resonance, the steady-state field enhancement $|E_{\mathrm{s}}/E_0|^2$ is proportional to the Q factor, where E_0 is the incident electric field amplitude. Consequently, the SHG and THG intensities can be expressed as:

$$I_{\mathrm{SHG}} \propto E^4 \propto Q^2\left[1 - e^{-(\frac{t}{\tau})}\right]^4, \tag{3}$$

$$I_{\mathrm{THG}} \propto E^6 \propto Q^3\left[1 - e^{-(\frac{t}{\tau})}\right]^6. \tag{4}$$

The normalized SHG and THG efficiencies as functions of Q factor are shown in Supplementary Fig. 3. An optimal value is found near Q = 130, beyond which the slow response of the cavity starts to limit the nonlinear enhancement. Considering nonradiative losses and fabrication tolerances in practical operation, a measured Q factor of approximately 100 offers a suitable balance between field enhancement and temporal matching, enabling efficient nonlinear generation under our experimental conditions.

Supplementary Note 4: Demonstration of local and nonlocal resonance origins

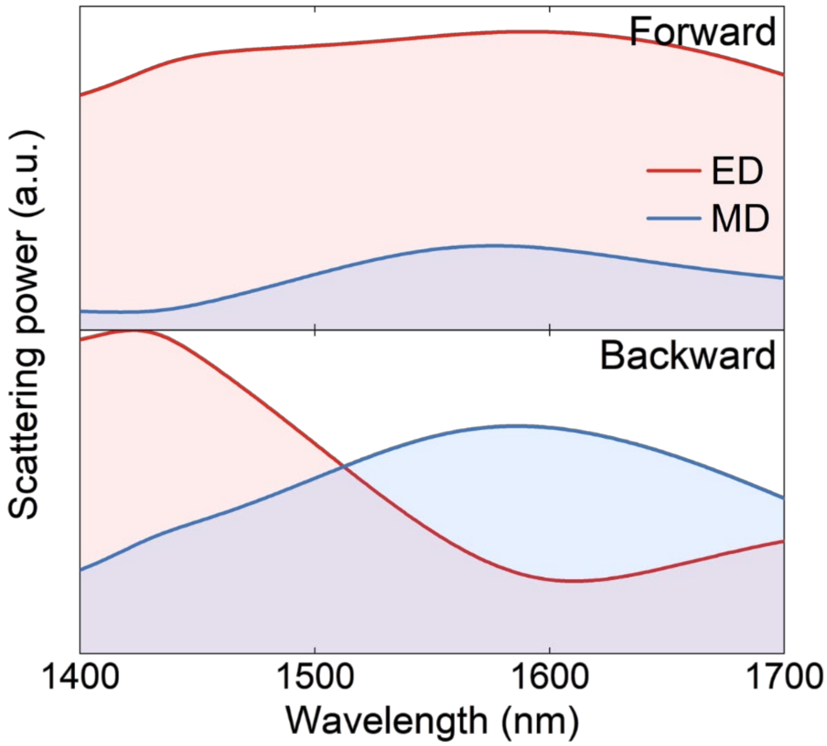

Supplementary Fig. 4: Demonstration of local and nonlocal resonance origins. Electric dipole (ED) and magnetic dipole (MD) contributions of the isolated IRU under forward and backward excitations.

To reveal the local and nonlocal characteristics of the two excited resonances, Supplementary Fig. 4 presents the electric dipole (ED) and magnetic dipole (MD) contributions of an isolated IRU under forward and backward excitations, where nonlocal coupling is absent. Only the low-Q resonance is observed at a wavelength of around 1580 nm, corresponding to the local resonance in Fig. 2c. In contrast, the high-Q quasi-bound state in the continuum (q-BIC) resonance is not excited in the isolated structure, confirming its nonlocal origin. Moreover, the differing dominant ED and MD contributions under forward and backward excitation suggest that the local resonance plays a significant role in the asymmetric response.

Supplementary Note 5: Simulated nonlinear spectral responses

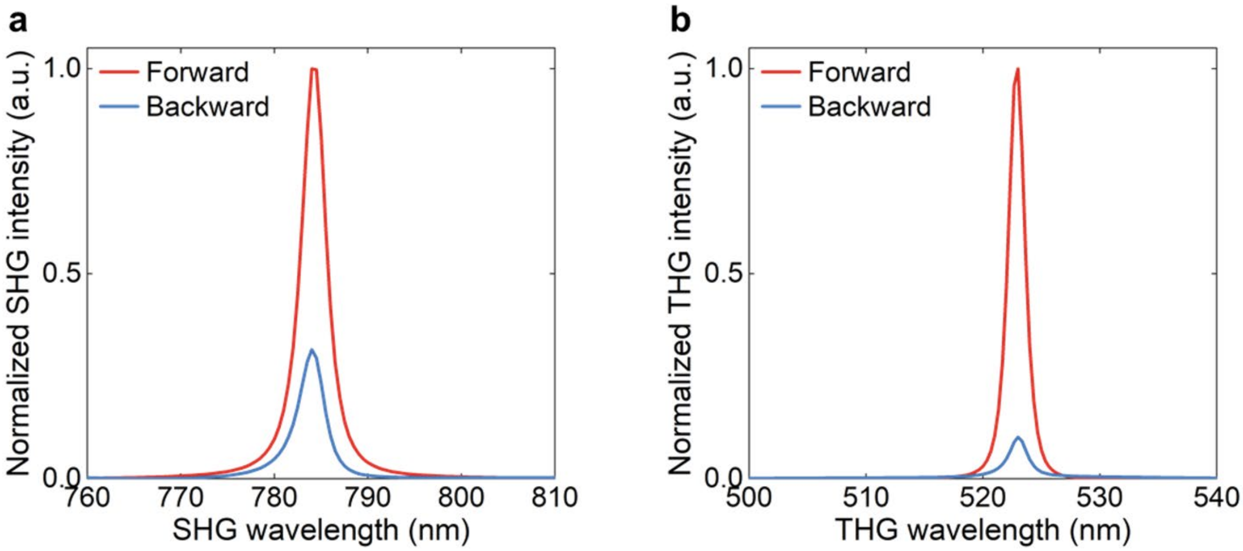

Supplementary Fig. 5: Simulated nonlinear spectral responses. a,**b**, Normalized simulated SHG (**a**) and THG (**b**) spectra under forward and backward excitations.

To simulate the SHG and THG responses, the nonlinear polarization of silicon is defined in the nonlinear physics module as:

$$\mathbf{P}^{(2)}_{\text{Surface}} = \varepsilon_0 \chi^{(2)}_{\text{Surface}} : \mathbf{EE}\,, \tag{5}$$

$$\mathbf{P}^{(3)} = \varepsilon_0 \chi^{(3)} \left(\mathbf{E}\cdot\mathbf{E}\right)\mathbf{E}\,, \tag{6}$$

where $\chi^{(2)}_{\perp\perp\perp}$ = 150×10^{-22} m^2/V and $\chi^{(2)}_{\|\perp\|} = \chi^{(2)}_{\|\|\perp}$ = 8.2×10^{-22} m^2/V are the second-order surface nonlinear susceptibilities, and $\chi^{(3)}$ = 2.45×10^{-19} m^2/V^2 is the third-order nonlinear susceptibility. **E** denotes the fundamental electric field. The nonlinear output intensity is calculated by performing a surface integral of the Poynting vector over the corresponding output plane.

Supplementary Note 6: Simulated phase profiles

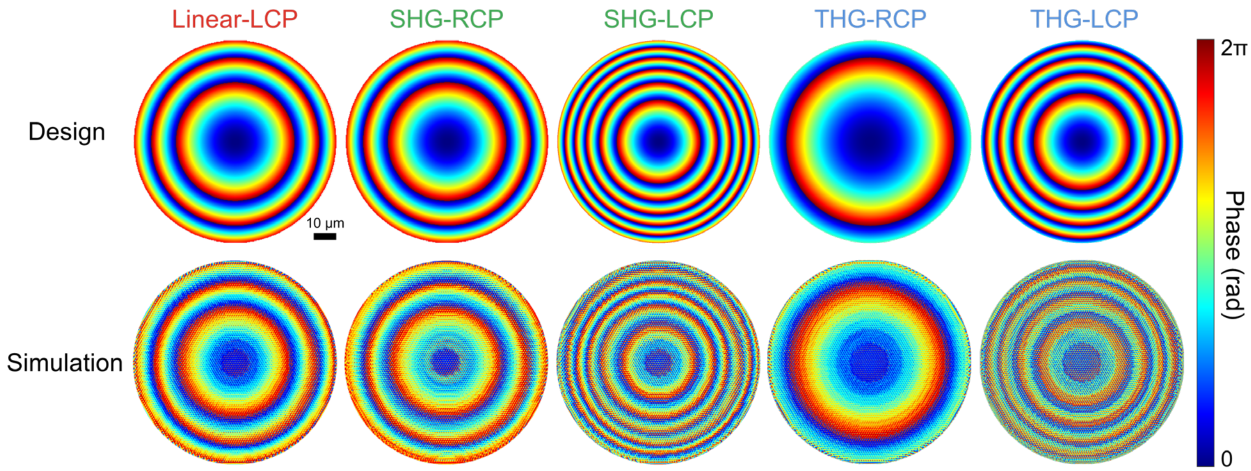

Supplementary Fig. 6: Designed and simulated phase profiles. Phase profiles of the proposed nonlocal meta-lens for linear, SHG, and THG with different circular polarizations.

To demonstrate that the designed phases are correctly implemented at their corresponding locations, the simulated phase distributions extracted from the nonlocal meta-lens for the linear, SHG, and THG cases are presented in Supplementary Fig. 6. The obtained phase distributions closely match the designed ones, demonstrating the potential for effective focusing capability. The minor nonuniformities arise from the limited mesh resolution, as the full-lens simulation involves an extremely large data volume, but they do not affect our conclusions.

Supplementary Note 7: Simulated light-field responses of harmonic generations

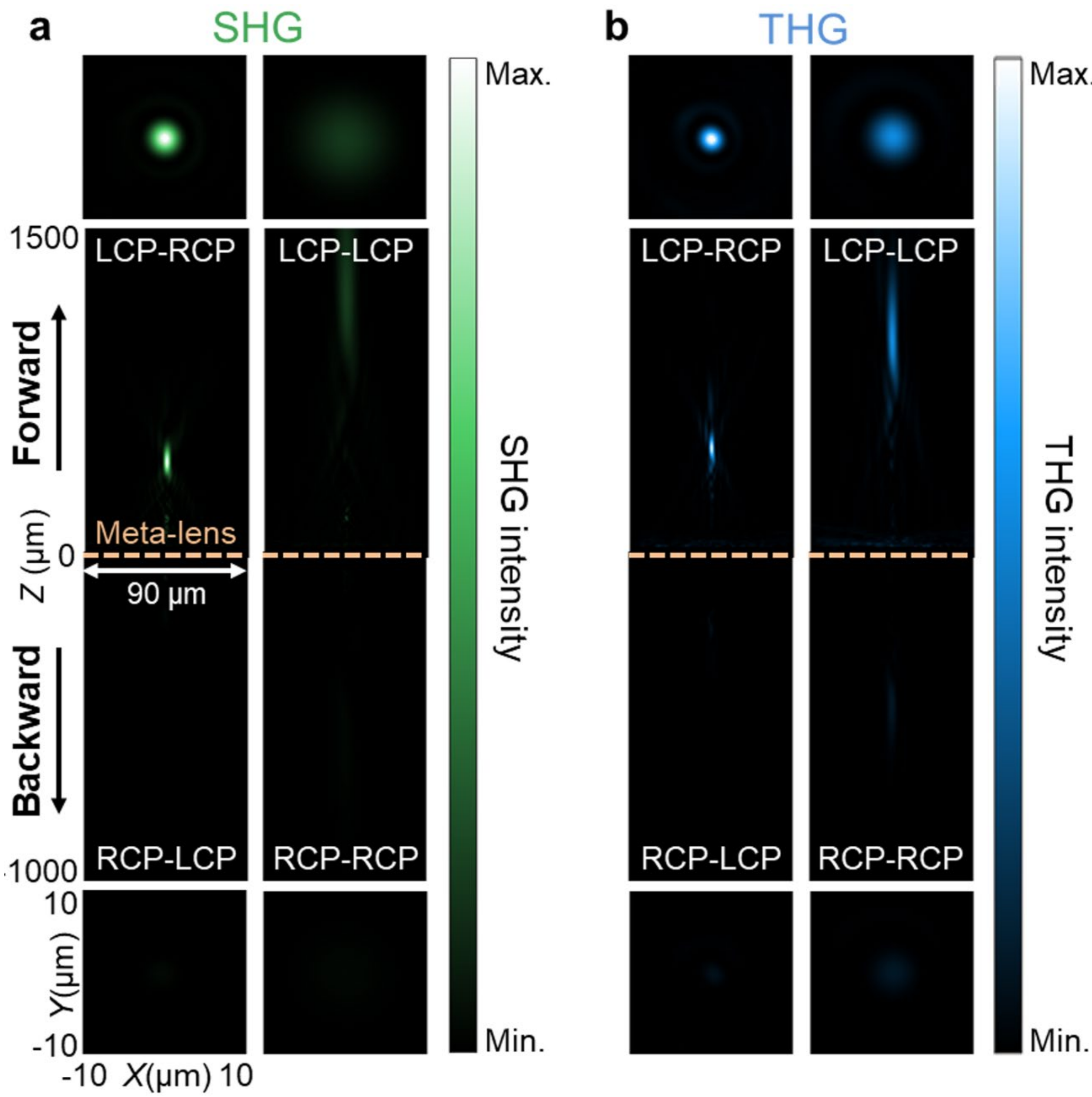

Supplementary Fig. 7: Simulated light-field responses of harmonic generations. a, Simulated *xz*- and *xy*-plane SHG focusing profiles under forward and backward excitations for two output circular polarization states. *Xy*-plane intensity profiles are extracted at the respective focal planes. **b**, Corresponding THG focusing profiles.

Supplementary Note 8: Simulated spectral responses at the fundamental wavelength

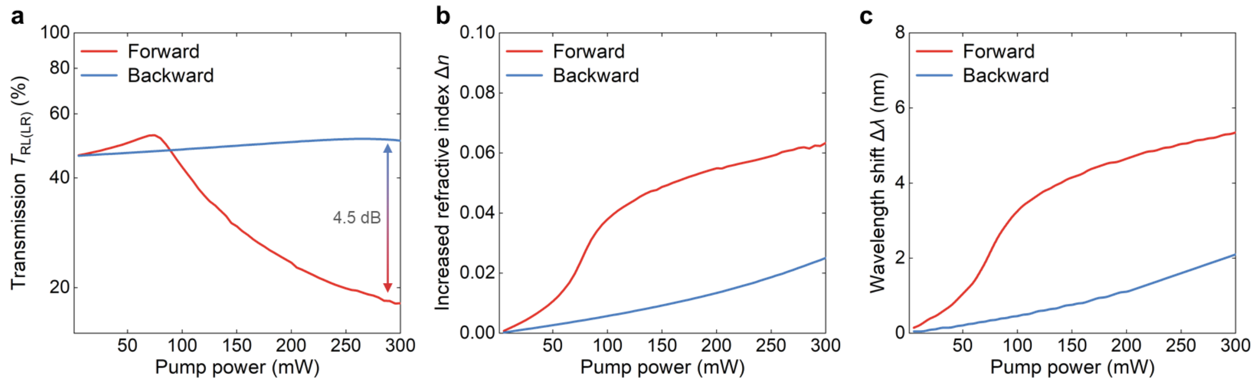

Supplementary Fig. 8: Simulated spectral responses at the fundamental wavelength. a,b,c, Simulated transmission polarization conversion efficiency $T_{RL(LR)}$ (**a**), averaged refractive index increase Δn within the silicon IRU (**b**), and wavelength shift $\Delta\lambda$ (**c**) as a function of pump power along forward and backward directions.

Supplementary Fig. 8 shows the simulated transmission polarization conversion efficiency $T_{RL(LR)}$, increased refractive index Δn, and wavelength shift $\Delta\lambda$ as a function of pump power along forward and backward directions. To better match the experimental conditions, the offset is set to $L = 300$ nm and the wavelength to $\lambda = 1630$ nm. The intensity-dependent refractive index ε_{NL} is modeled as

$$\varepsilon_{NL} = \varepsilon_L + \chi_{eff}^{(3)} |E|^2, \quad (7)$$

where ε_L is the linear permittivity of silicon, and $\chi_{eff}^{(3)} = 8\times10^{-15}$ m^2/V^2 is the effective intensity-dependent nonlinear susceptibility. This value is four orders of magnitude higher than the intrinsic transient nonlinearity used in Supplementary Note 5. This is because the nonlinear refractive index change discussed in our work originates from the thermo-optic effect, which is a stable or quasi-stable process governed by the average pump intensity. The transient Kerr effect, which depends on the peak pump intensity, is not considered here, as our measurements do not involve ultrafast time-resolved characterization. With increasing pump power, the forward direction exhibits a larger refractive index increase and a correspondingly greater wavelength shift, leading to a more rapid decrease in transmission. When the pump power exceeds 100 mW, the forward transmission decreases significantly because the designed resonance is perturbed, while the backward transmission remains nearly unchanged at around 50%, yielding a transmission ratio of approximately 2.8 (4.5 dB) at a pump power of 300 mW. The minor deviation between simulation and experiment may originate from intensity-dependent absorption effects (e.g., thermally induced two-photon absorption) and the spectral bandwidth of the laser (~20 nm), which causes averaging effects over multiple wavelengths. Additional factors, such as slight focusing and incident angle deviations of the pump light, also influence the results. More details are elaborated in Supplementary Note 11.

Supplementary Note 9: Relation between efficiency and asymmetry contrast

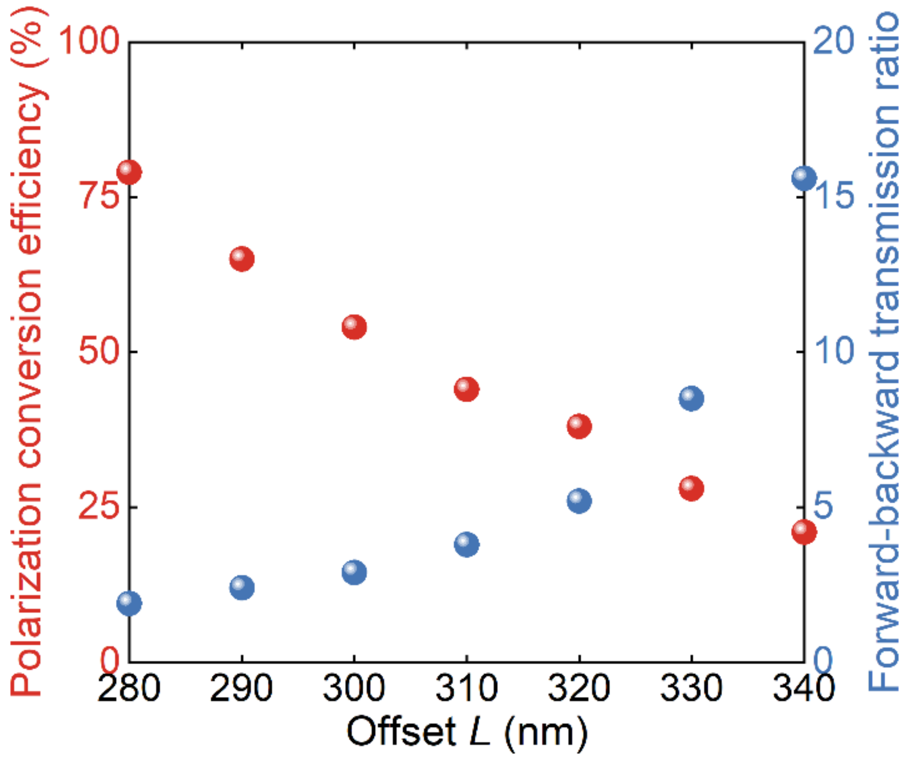

Supplementary Fig. 9: Relation between efficiency and asymmetry contrast. Simulated polarization conversion efficiency and forward-backward transmission ratio with varying offset *L*.

In addition to the three key factors of high nonlinear efficiency, precise wavefront shaping, and strong directional asymmetry, high efficiency at the fundamental wavelength is also required to be additionally considered, which inevitably influences the design for high intensity asymmetry. There are two theoretical limits for circularly polarized asymmetric responses. The first is the transmission polarization conversion efficiency of approximately 25% in ultrathin metasurfaces, which has been overcome in the previous work[1]. The second is the asymmetric transmission limit[2] of $4NRIR/(NRIR+1)^2$. Taking both limits into account and given that our experimental value of NRIR is approximately 3, the theoretical efficiency limit for a single-mode ultrathin metasurface is about 18.75%. Benefiting from Fano-like coupling between local and nonlocal resonances, our design achieves a high experimental polarization conversion efficiency of approximately 60%, surpassing this theoretical bound. Supplementary Fig. 9 analyzes the correlation between polarization conversion efficiency and the forward-to-backward transmission ratio. As the offset L increases, the coupling strength between local and nonlocal resonances is tuned, resulting in a gradual reduction of efficiency while effectively enhancing the forward-to-backward transmission ratio. A high ratio of 15.6 (11.9 dB) is achieved at L = 340 nm, where the efficiency remains 21%, still exceeding the theoretical limit of 18.75%. We note that an intrinsic balance exists between efficiency and contrast ratio, representing an inevitable trade-off to be further optimized in future studies. Our present work primarily focuses on overcoming the trade-offs among nonlinear conversion efficiency, wavefront shaping capability, and directional asymmetry, while achieving their simultaneous operation at the fundamental, SHG, and THG wavelengths.

Supplementary Note 10: Asymmetric response dependence on substrate refractive index

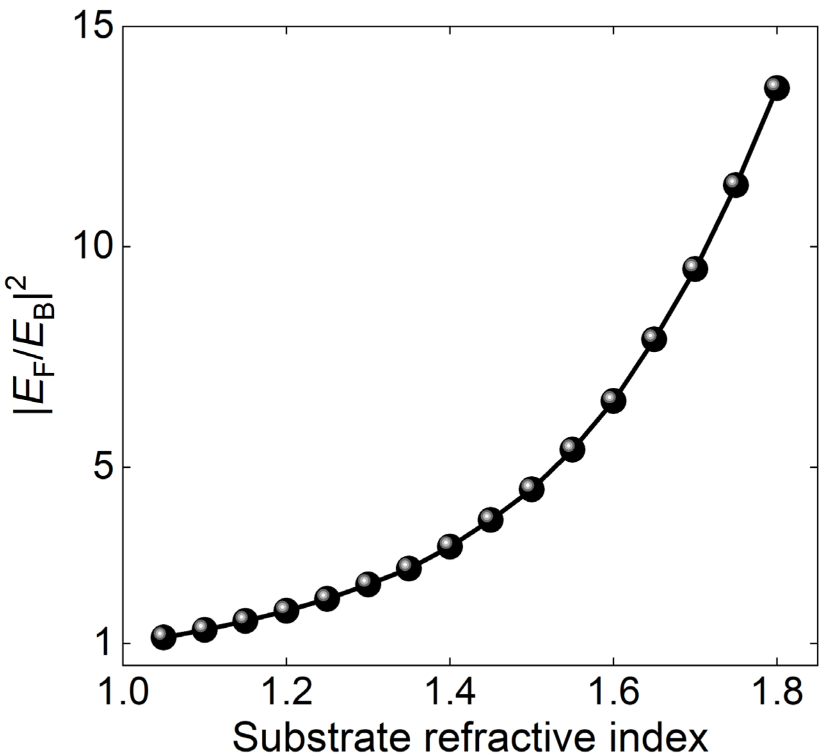

Supplementary Fig. 10: Asymmetric response dependence on the substrate. Asymmetric electric field enhancement $|E_F/E_B|^2$ as a function of substrate refractive index.

Supplementary Fig. 10 shows the asymmetric electric field enhancement $|E_F/E_B|^2$ as a function of the substrate refractive index. The proposed meta-lens and the underlying asymmetry-enhancement mechanism remain effective across a range of substrate refractive indices. As the refractive index increases to 1.8, the asymmetry is significantly amplified, reaching a high value of 13.6. It is worth noting that the design is also applicable to substrates with even higher refractive indices, although this would require further optimization of other geometric parameters.

Supplementary Note 11: Angular dependence of field enhancement

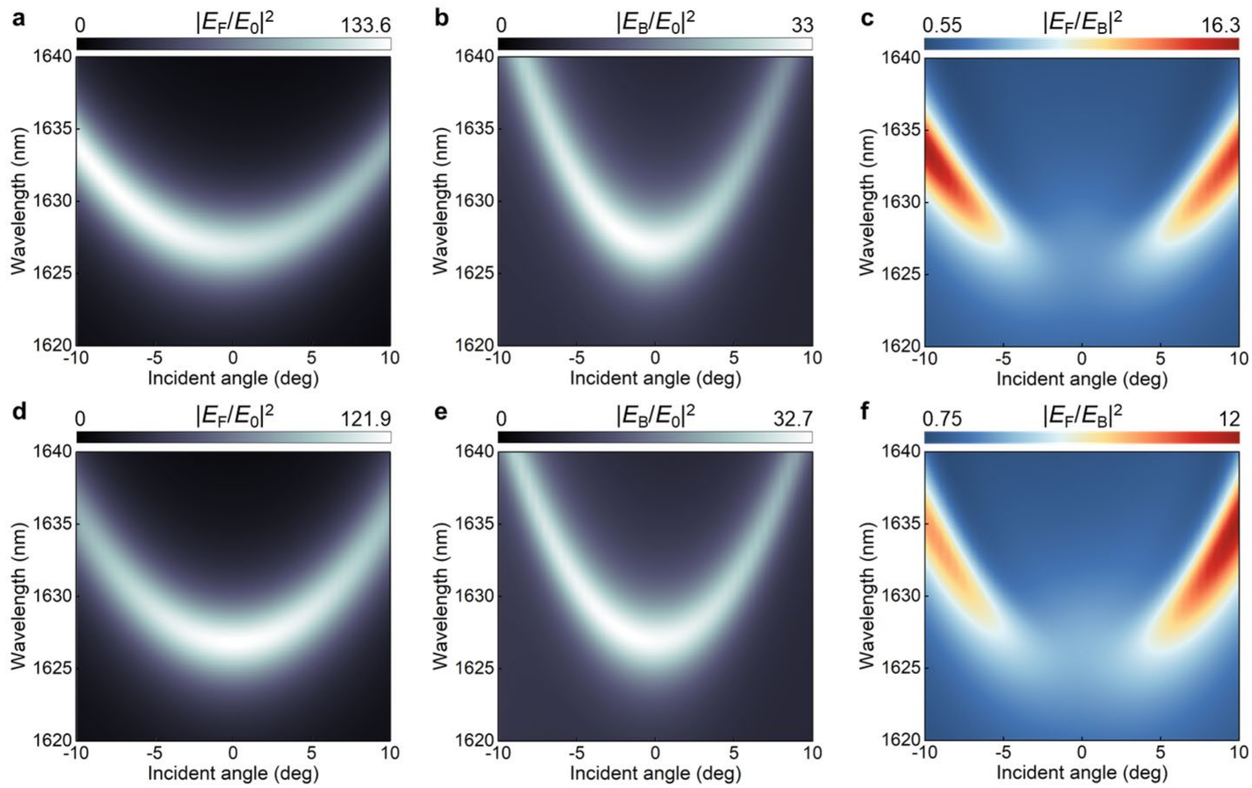

Supplementary Fig. 11: Angular dependence of field enhancement. a-c, Incident-angle dependence of the normalized electric field enhancements $|E_F/E_0|^2$ (**a**), $|E_B/E_0|^2$ (**b**), and the forward-to-backward ratio $|E_F/E_B|^2$ (**c**) in the *xoz* plane. **d-f**, Corresponding results in the *yoz* plane.

Since the proposed meta-lens operates based on nonlocal effects, its angular dispersion should be carefully investigated. Supplementary Fig. 11 presents the incident-angle dependence of the normalized electric field enhancements $|E_F/E_0|^2$, $|E_B/E_0|^2$, and the forward-to-backward ratio $|E_F/E_B|^2$ in *xoz* and *yoz* planes, where E_F, E_B, and E_0 represent the forward-propagating, backward-propagating, and incident electric field amplitudes, respectively. The *xyz* coordinates follow the same convention as in Fig. 2c. Due to the refractive index difference between air and silica, the incident wavevectors differ for forward and backward excitations, leading to distinct transverse wavevector components. As a result, the nonlocal resonances exhibit direction-dependent angular responses. This angular dependence further enhances the asymmetry in near-field excitation. Notably, the maximum forward-to-backward electric field enhancement ratio $|E_F/E_B|^2$ reaches 16.3 at an oblique incidence of 10°, exceeding the value of 3.8 observed under normal incidence. Moreover, this ratio can be further increased by adopting a larger incident angle, providing a promising route toward highly asymmetric meta-devices.

Supplementary Note 12: Performance comparison

Table S1. Metasurface performance comparison for nonlinear processes: generation efficiency, wavefront shaping, and directional asymmetry.

References	THG efficiency η	Normalized THG efficiency η/I_{pump}^2 (cm^4/GW^2)	Wavefront	Directional asymmetry
Ref. 3	1.2×10^{-6}	1.17×10^{-7}	/	/
Ref. 4	1×10^{-6}	1.49×10^{-7}	/	/
Ref. 5	9.1×10^{-7}	9.1×10^{-5}	/	/
Ref. 6	1×10^{-11}	1.49×10^{-9}	√	/
Ref. 7	1.1×10^{-6}	1.01×10^{-9}	√	/
Ref. 8	2.65×10^{-5}	2.5×10^{-7}	√	/
Ref. 9	7.92×10^{-9}	3.57×10^{-7}	/	√
This work	2.9×10^{-6}	1.56×10^{-6} (Saturated) 6.35×10^{-6} (Unsaturated)	√	√

Supplementary references

1. Yao J. et al. Nonlocal meta-lens with Huygens' bound states in the continuum. *Nat. Commun.* **15**, 6543 (2024).

2. Cotrufo M., Cordaro A., Sounas D. L., Polman A., Alù A. Passive bias-free non-reciprocal metasurfaces based on thermally nonlinear quasi-bound states in the continuum. *Nat. Photonics* **18**, 81-90 (2024).

3. Yang Y. et al. Nonlinear Fano-resonant dielectric metasurfaces. *Nano Lett.* **15**, 7388-7393 (2015).

4. Koshelev K. et al. Nonlinear Metasurfaces Governed by Bound States in the Continuum. *ACS Photonics* **6**, 1639-1644 (2019).

5. Liu Z. et al. High-Q Quasibound States in the Continuum for Nonlinear Metasurfaces. *Phys. Rev. Lett.* **123**, 253901 (2019).

6. Reineke B. et al. Silicon metasurfaces for third harmonic geometric phase manipulation and multiplexed holography. *Nano Lett.* **19**, 6585-6591 (2019).

7. Gao Y. et al. Nonlinear Holographic All-Dielectric Metasurfaces. *Nano Lett.* **18**, 8054-8061 (2018).

8. Hail C. U., Michaeli L., Atwater H. A. Third Harmonic Generation Enhancement and Wavefront Control Using a Local High-Q Metasurface. *Nano Lett.* **24**, 2257-2263 (2024).

9. Kruk S. S. et al. Asymmetric parametric generation of images with nonlinear dielectric metasurfaces. *Nat. Photonics* **16**, 561-565 (2022).